

www.acsami.org Research Article

Damage-Free Atomic Layer Etch of WSe₂: A Platform for Fabricating Clean Two-Dimensional Devices

Ankur Nipane,*, Min Sup Choi,*, Punnu Jose Sebastian, Kaiyuan Yao, Abhinandan Borah, Prathmesh Deshmukh, Younghun Jung, Bumho Kim, Anjaly Rajendran, Kevin W. C. Kwock, Amirali Zangiabadi, Vinod M. Menon, P. James Schuck, Won Jong Yoo, James Hone, and James T. Teherani*



Cite This: ACS Appl. Mater. Interfaces 2021, 13, 1930-1942



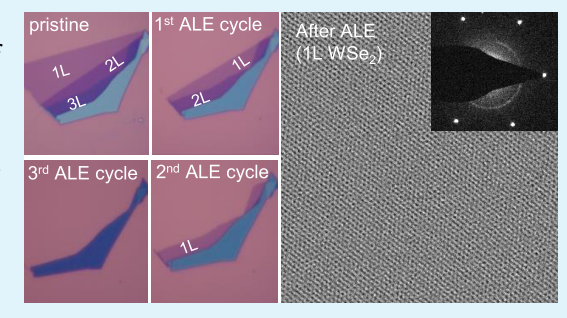
ACCESS I

Metrics & More

Article Recommendations

SI Supporting Information

ABSTRACT: The development of a controllable, selective, and repeatable etch process is crucial for controlling the layer thickness and patterning of two-dimensional (2D) materials. However, the atomically thin dimensions and high structural similarity of different 2D materials make it difficult to adapt conventional thin-film etch processes. In this work, we propose a selective, damage-free atomic layer etch (ALE) that enables layer-by-layer removal of monolayer WSe₂ without altering the physical, optical, and electronic properties of the underlying layers. The etch uses a top-down approach where the topmost layer is oxidized in a self-limited manner and then removed using a selective etch. Using a comprehensive set of material, optical, and electrical characterization, we show that the quality of our ALE



processed layers is comparable to that of pristine layers of similar thickness. The ALE processed WSe₂ layers preserve their bright photoluminescence characteristics and possess high room-temperature hole mobilities of 515 cm²/V·s, essential for fabricating high-performance 2D devices. Further, using graphene as a testbed, we demonstrate the fabrication of ultra-clean 2D devices using a sacrificial monolayer WSe₂ layer to protect the channel during processing, which is etched in the final process step in a technique we call sacrificial WSe₂ with ALE processing (SWAP). The graphene transistors made using the SWAP technique demonstrate high room-temperature field-effect mobilities, up to 200,000 cm²/V·s, better than previously reported unencapsulated graphene devices.

KEYWORDS: atomic layer etch, layer-by-layer etch, self-limiting oxidation, WSe2, graphene

■ INTRODUCTION

Etching is one of the cornerstones of modern semiconductor device processing. The development of suitable etching techniques is essential for fabrication and large-scale integration of next-generation devices. In this regard, atomic layer etching methods become critical to advance devices made from 2D materials, such as graphene and transition metal dichalcogenides (TMDCs), as their optical and electronic properties change with layer thickness.^{1,2} Controllable etching is also required for reliable patterning, clean layer transfers, and high-quality ohmic contacts to 2D materials.^{3,4} Although etching of conventional bulk materials has demonstrated reliable sub-10 nm resolution, etching methods for twodimensional (2D) materials are still in their infancy. Controllable etching of 2D materials has been a challenging task due to the presence of large surface-to-volume ratios (such that any surface damage readily impacts device performance), high structural similarity between different 2D materials, and lack of a suitable etch-stop layer.

To date, several etching techniques have been proposed to control the layer number and patterning of 2D materials. These techniques involve high-energy lasers, focused-ion beams, thermal/vacuum annealing, gaseous-phase surface treatments, and plasma-based etching. High-energy lasers and focused-ion beams have shown to be effective for controlled etching of MoS₂; however, these techniques are limited by their throughput and limited scalability.^{6,7} Thermal/vacuum annealing and gaseous-phase surface treatments offer a fast, repeatable, and wafer-scale etching process and have been widely used to etch various TMDCs such as MoS₂ and WSe₂.^{8,9} However, detailed electrical and optical characterization of the etched flakes, required to support their suitability in device applications, has been lacking.

Meanwhile, a wide range of plasma-based etching techniques has been developed for 2D materials due to their high

Received: October 13, 2020 Accepted: December 8, 2020 Published: December 22, 2020





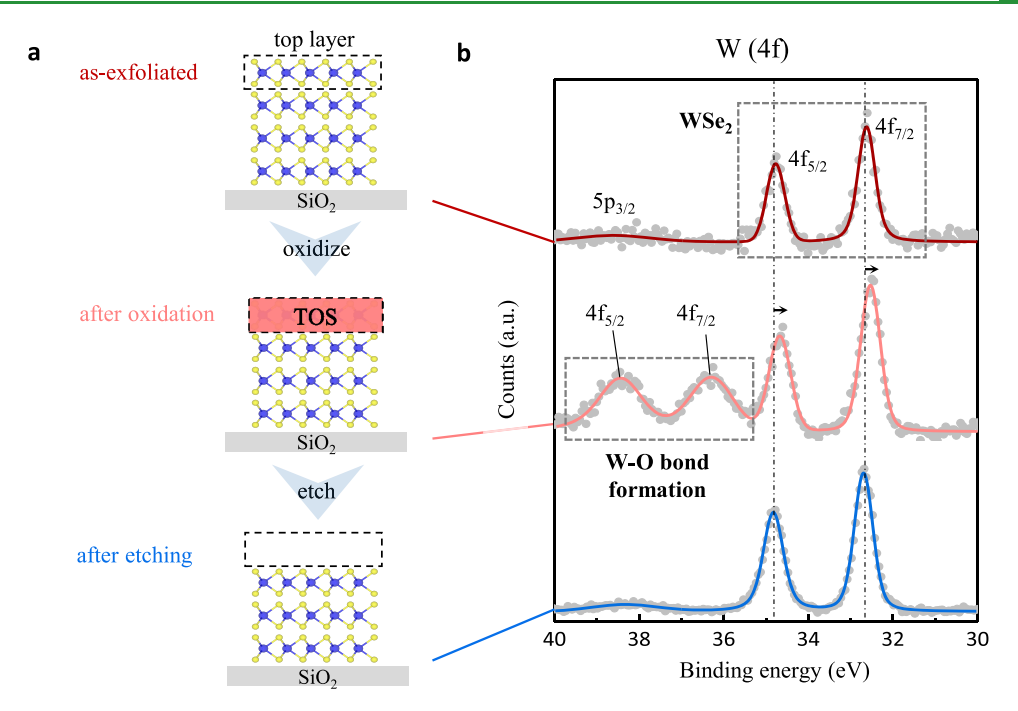


Figure 1. ALE process flow and XPS characterization. (a) The topmost layer of WSe_2 is removed by first oxidizing the flake using $UV+O_3$ for 30 min at room temperature, forming monolayer tungsten oxyselenide (TOS) that is subsequently removed with a mild 10 s dip in 1M KOH solution. The etching process selectively removes the topmost oxidized layer without damaging the underlying layers. (b) XPS spectra of the W (4f) peak for a 4L WSe_2 flake showing the appearance of W-O peaks after the UV-ozone process. The peaks corresponding to W-O bond formation disappears after the KOH treatment, indicating the removal of the TOS layer.

throughput, low variability, and CMOS compatibility. In this regard, some of the earliest works involved the development of hydrogen-plasma etching methods for selective patterning of graphene edges over the basal plane for advanced nanoribbon devices. 10-1 These techniques were then expanded to other low-dimensional materials such as carbon nanotubes (CNTs) and MoS2 where plasma-based surface treatments were used to perform defect annealing and create high-efficiency hydrogen evolution reaction (HER) sites. 13-16 Subsequently, soft-plasma etching techniques were developed to achieve layer-by-layer etching of graphene and MoS₂. These methods provide great control on the thickness with minimal damage to the etched layers. However, most plasma-based layer-by-layer etching techniques are not self-limiting in nature due to associated physical etch and thus require careful optimization of several parameters such as plasma density, sample distance from the plasma source, and etching time to achieve monolayer precision.²

In this article, we introduce a clean, area-selective, and damage-free atomic layer etch that overcomes the aforementioned issues of existing techniques for etching 2D materials. Our ALE process is a top-down approach that involves cyclical steps of self-limited oxidation and selective etch to achieve the desirable layer thickness. We chose tungsten diselenide (WSe₂) as a platform for demonstrating the ALE process due to the widespread interest in its unique properties such as high quantum yield, large spin-orbit coupling, and ambipolar charge transport. In addition, our method employs a wafer-scale, room-temperature process with the potential of having high throughput for use in back-end-of-the-line (BEOL) integration.

Furthermore, using graphene as a testbed, we demonstrate that our ALE process enables etching and cleaning of the top surface of the channel after device fabrication resulting in pristine high-quality 2D devices. Generally, high-quality 2D devices are fabricated using a dry/wet transfer of mechanically exfoliated or chemical vapor deposition (CVD)-grown 2D materials on insulating hexagonal boron nitride (h-BN). However, these transfer processes are marred by large surface contamination, unintentional trapping of residues, and nonhomogeneous topography, which results in poor device performance and large device-to-device variability.²⁵ Here, we use monolayer WSe2 as a first-of-its-kind sacrificial 2D layer to protect the surface of a monolayer graphene transistor from any polymer residue during different fabrication steps. We finally remove the sacrificial WSe2 layer with ALE processing (SWAP) technique and demonstrate high-quality graphene transistors with field-effect mobilities 3× than our control devices fabricated using direct polymer-based transfer technique.

■ RESULTS AND DISCUSSION

As shown in Figure 1a, our ALE process consists of two distinct steps:

- 1. Self-limited oxidation of the topmost WSe₂ layer. The sample is exposed to ozone (O₃) under ultraviolet (UV) light for 30 min at room temperature.
- 2. Selective etching of the oxidized layer. The sample is dipped in a 1 M potassium hydroxide (KOH) solution for 10 s and then rinsed with DI water.

In the first step, UV-ozone exposure converts the topmost WSe_2 layer into monolayer tungsten oxyselenide (TOS). The UV-ozone oxidation was performed in SAMCO UV-2 system, a commercially available UV-ozone cleaning/stripping tool. The process was performed at room temperature with an oxygen flow rate of 3 L/min. The oxidation process starts with the dissociation of O_3 into molecular oxygen (O_2) and singlet

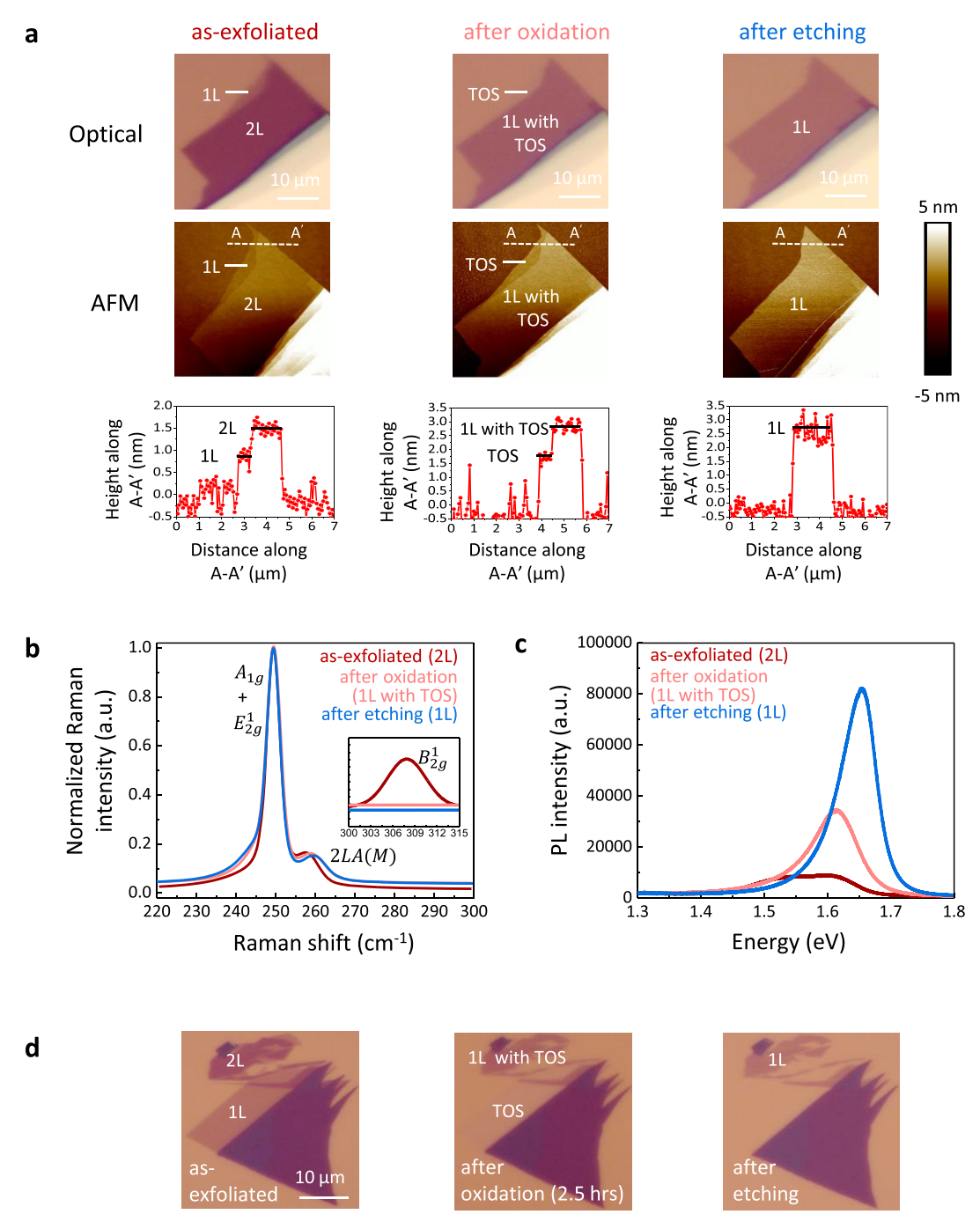


Figure 2. Monolayer precision of the ALE process. (a) Optical images (top), AFM scans (middle), and height profiles (bottom) of an exfoliated WSe₂ flake on SiO₂ at each stage of the ALE process. The as-exfoliated bilayer region (2L) is etched down to monolayer (1L), and the monolayer region is completely removed after the oxidation and etching step. (b) Raman spectra for the as-exfoliated, oxidized, and etched flake from (a). The Raman spectra were taken near the center of the 2L region of the flake. The removal of the B_{2g}^1 peak (in the inset) corroborates the conversion from a bilayer to a monolayer. (c) PL spectra are taken from the as-exfoliated bilayer region of the flake given in (a) at each stage of the ALE process. The PL spectra show a clear transition from a broad, low intensity bilayer spectrum to a sharp, high-intensity monolayer spectrum, in agreement with our optical and AFM results. (d) Optical images highlighting the self-limiting nature of our oxidation process. Only a single layer of WSe₂ is removed despite using a (5×) longer oxidation process (2.5 h).

oxygen radical (O $^{(1)}$ D) in the presence of UV light. Then, the singlet oxygen radical (a strong oxidizing agent) reacts with the topmost WSe₂ layer to give monolayer TOS in a self-limited manner. This process is similar to that used by commercial UV-ozone cleaners to remove organic polymers from the surfaces of bulk semiconductors.

To confirm the presence of TOS, we performed X-ray photoelectron spectroscopy (XPS) on a four-layer (4L) WSe₂

flake stacked on a thick h-BN flake using the polycaprolactone (PCL) polymer-based dry transfer process. Figure 1b shows the XPS spectra for the tungsten (W (4f)) core level at each stage of the ALE process. Compared to the as-exfoliated sample, the spectra for the oxidized sample show two additional weak doublet peaks at higher binding energies. These higher energy doublet peaks correspond to the formation of W–O bonds, similar to that of tungsten oxide

(WO_x) observed in a previous work.²⁷ Additionally, the presence of stronger doublet peaks corresponding to WSe2 in the oxidized sample indicates that our oxidation process only affects the topmost layer. This is further confirmed by Raman and photoluminescence (PL) measurements, which are discussed in the subsequent sections. The slight redshift in the binding energies of the WSe2 peaks after oxidation can be attributed to the doping of the underlying layers due to the presence of the TOS layer on top.²⁸ To confirm that the oxidation produces a homogeneous layer of TOS, we oxidized a 1L WSe2 flake, as shown in Figure S1. Our method produces a clean, continuous oxide film after UV-ozone exposure, which was confirmed using optical and atomic force microscopy (AFM) techniques. Our Raman measurements on the same oxidized monolayer sample (Figure S2), depict the amorphous nature of the top TOS layer as no Raman peak between 790-810 cm $^{-1}$ (indicative of crystalline WO_x) was observed.²⁹

In the second step, we dip the oxidized samples in a 1 molar (M) KOH solution to selectively remove the topmost TOS layer. KOH has been previously shown to selectively remove tungsten oxide (WO_r) without etching the underlying WSe₂ layers.³⁰ We then rinse the etched samples with DI water to completely remove KOH traces from the surface. As detailed in the following sections, the underlying layers are not affected by this mild etching process. XPS spectra for the etched sample show that the doublet peaks corresponding to the TOS layer are completely removed after KOH treatment, while the peaks corresponding to WSe2 peaks are restored to their pristine form (no shift in binding energy compared to the as-exfoliated sample). The above steps can be repeated in a cyclical manner to remove the desired number of layers of WSe2 as shown in Figure S3. Exactly one layer is removed per ALE cycle with minimal damage (if any) to the etched layers as shown by the Raman and PL characterization. Furthermore, we demonstrate that our ALE process is area-selective by removing WSe2 layers from a particular section of a few-layer flake (Figure S4) by using a poly(methyl methacrylate) (PMMA) mask. This shows that our ALE process is patternable and can be used to selectively remove WSe2 layers from a particular area to create novel 2D structures.

To further support our claim of monolayer precision, we investigated a WSe₂ flake exfoliated on a 285 nm SiO₂/Si substrate with naturally abutting monolayer (1L) and bilayer (2L) regions. Figure 2a shows the optical and AFM images of the flake at each stage of the ALE process. The optical contrast of the entire flake changes significantly after oxidation such that the oxidized 1L region (labeled TOS) is nearly indistinguishable from the substrate and the oxidized 2L region (labeled 1L with TOS) is visually similar to 1L WSe₂. The corresponding AFM images for the oxidized samples show the presence of both bilayer and monolayer regions of the flake after oxidation when compared to the as-exfoliated flake, which confirms that the change in optical contrast is due to oxidation rather than etching of the top layer. This is also evident when we study the height (thickness) profiles where, rather than a decrease, we observe an increase in thickness of both 1L and 2L regions after oxidation that corresponds to the creation of the TOS layer with a different bonding configuration. Subsequently, the flake undergoes the etching step after which the monolayer region is completely removed and the bilayer region is thinned down to monolayer with no apparent change in the shape or size. The similarity in the optical contrast between the etched-to monolayer (bilayer etched to a

monolayer) and the oxidized bilayer further confirms that only the top layer gets oxidized in our process. Note that the relative increase in height of the etched-to monolayer to that of the as-exfoliated monolayer can be attributed to the etching of the neighboring SiO_2 region. We further confirmed this by comparing the thickness of the pristine and etched-to monolayers on an h-BN substrate, which depicts a similar thickness as shown in Figure S5.

Next, we performed Raman and photoluminescence characterization on the same flake to corroborate our optical and AFM results. Figure 2b shows the Raman spectrum of the as-exfoliated bilayer region at different steps of the ALE process. For the pristine bilayer (indicated in dark red), the dominant peak occurs at a Raman frequency of 249.42 cm⁻¹, which corresponds to the convoluted $A_{1g} + E_{2g}^1$ peak, where A_{1g} represents out-of-plane and E^1_{2g} represents in-plane vibrational modes. These modes are indistinguishable in our experiment since we have employed an unpolarized laser and thus can only be distinguished using curve fitting.³¹ Along with this, a secondary peak occurs at 258.12 cm^{-1} , known as the 2LA(M)peak, which represents the double resonance process involving two phonons from the longitudinal acoustic (LA) branch. Both $A_{1\sigma} + E_{2\sigma}^1$ and 2LA(M) peaks are present after oxidation, which confirms that the oxidation process only affects the top layer. The monolayer precision of our ALE process can be further corroborated by looking at the Raman mode (B_{2g}^1) , which is active only in few-layer WSe₂.³² As shown in the inset, the B_{2g}^1 peak occurs at 308.32 cm⁻¹ for the as-exfoliated 2L flake but disappears after the oxidation step indicating that only the top layer gets oxidized. Finally, both $A_{1g} + E_{2g}^1$ and 2LA(M) peaks remain strong after etching with 1.74 $\rm cm^{-1}$ blueshift in the 2LA(M) peak. The strong blueshift of the 2LA(M) peak is consistent with bilayer to monolayer transition. This confirms that the oxidation step only affects the topmost layer and the etching step selectively removes the top TOS layer.

Figure 2c shows the PL spectrum for the same flake at each stage of the ALE process. Here, we observe a clear transition from a low-intensity, double-peak spectrum for the asexfoliated bilayer region to a high-intensity single-peak spectrum (10× the peak intensity of original bilayer region) after etching. This increase in intensity and the peak shift toward a higher energy suggest a transition from indirect (bilayer) to direct bandgap (etched-to monolayer), confirming the monolayer precision of our ALE process. Meanwhile, the PL spectrum for oxidized bilayer looks similar to that of the etched-to monolayer though with a large redshift (45 meV) that can be attributed to p-type doping of the underlying layer.³³ Finally, Figure 2d shows the color-corrected optical images of a WSe2 flake used to demonstrate the self-limiting nature of our oxidation process. Here, even after employing a substantially longer oxidation process (5x than the usual 30 min duration), only the top 1L WSe₂ (indicated as 1L TOS) layer got oxidized. The self-limiting nature of the oxidation process has been previously studied using first-principle density functional theory (DFT) calculations where it was shown that the top layer (surface) of TMDCs have high affinity for oxidation in the presence of oxygen radicals; however, once the top layer gets fully oxidized, it creates a high vertical diffusion barrier for further oxidation due to strong and directional bonding between oxygen and chalcogen atoms, akin to the native SiO₂-Si interface.^{34,35} Similar self-liming oxidation of TMDCs using low-energy oxidation processes have been demonstrated in previous works. 36,37 It is noted that the ALE

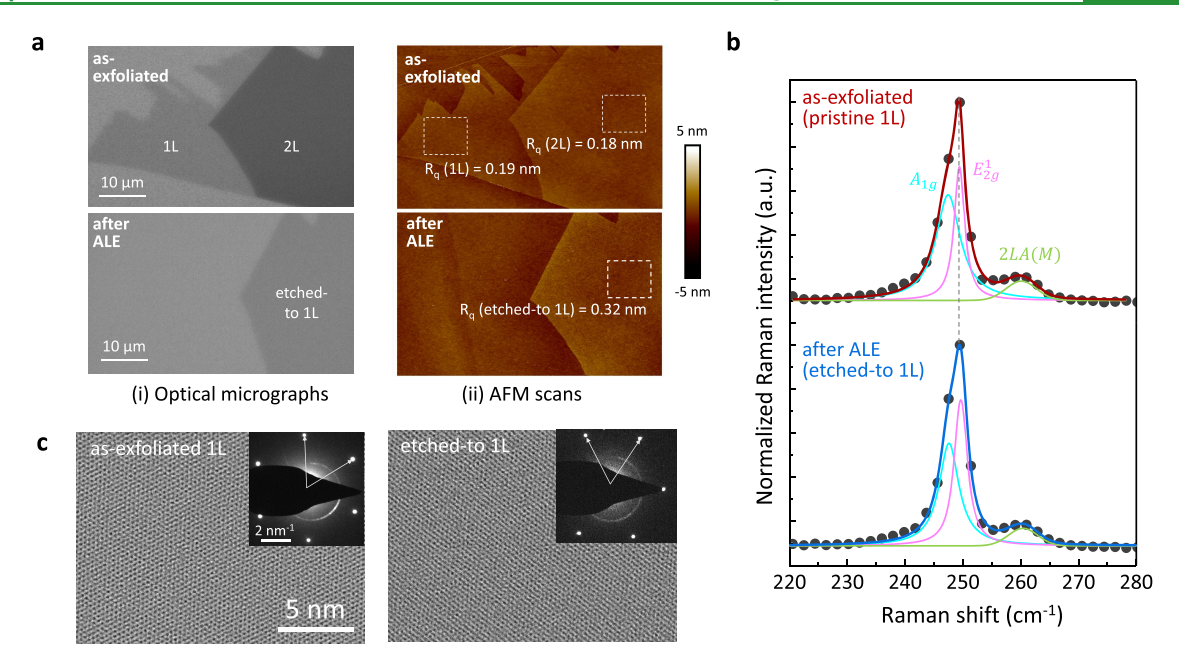


Figure 3. Comparison of pristine and etched-to 1L WSe₂ flakes. (a) (i) Optical images of WSe₂ flakes confirming the monolayer etch. The as-exfoliated bilayer (2L) region is etched down to monolayer (1L), and the monolayer region is completely removed. (ii) AFM characterization confirms the atomic layer etch with no apparent change in shape, size, or topography of the flake. RMS surface roughness (R_q) of the etched-to 1L is similar to that of the as-exfoliated monolayer, indicating that the ALE process minimally affects the underlying layers. (b) Raman spectrum of the etched-to 1L WSe₂ is similar to that of as-exfoliated 1L WSe₂. No additional defect peaks were observed in the etched-to 1L WSe₂ with negligible change in the peak positions, confirming the crystalline nature of the etched layers. (c) STEM images of as-exfoliated and etched-to 1L WSe₂ taken at the same scale. The etched flake does not show any noticeable damage or defects when compared to the pristine flake. The electron diffraction patterns also indicate the single-crystal structure of the etched-to 1L flake with a similar angle and distance between adjacent planes as that of pristine 1L WSe₂, as indicated by arrows in the inset.

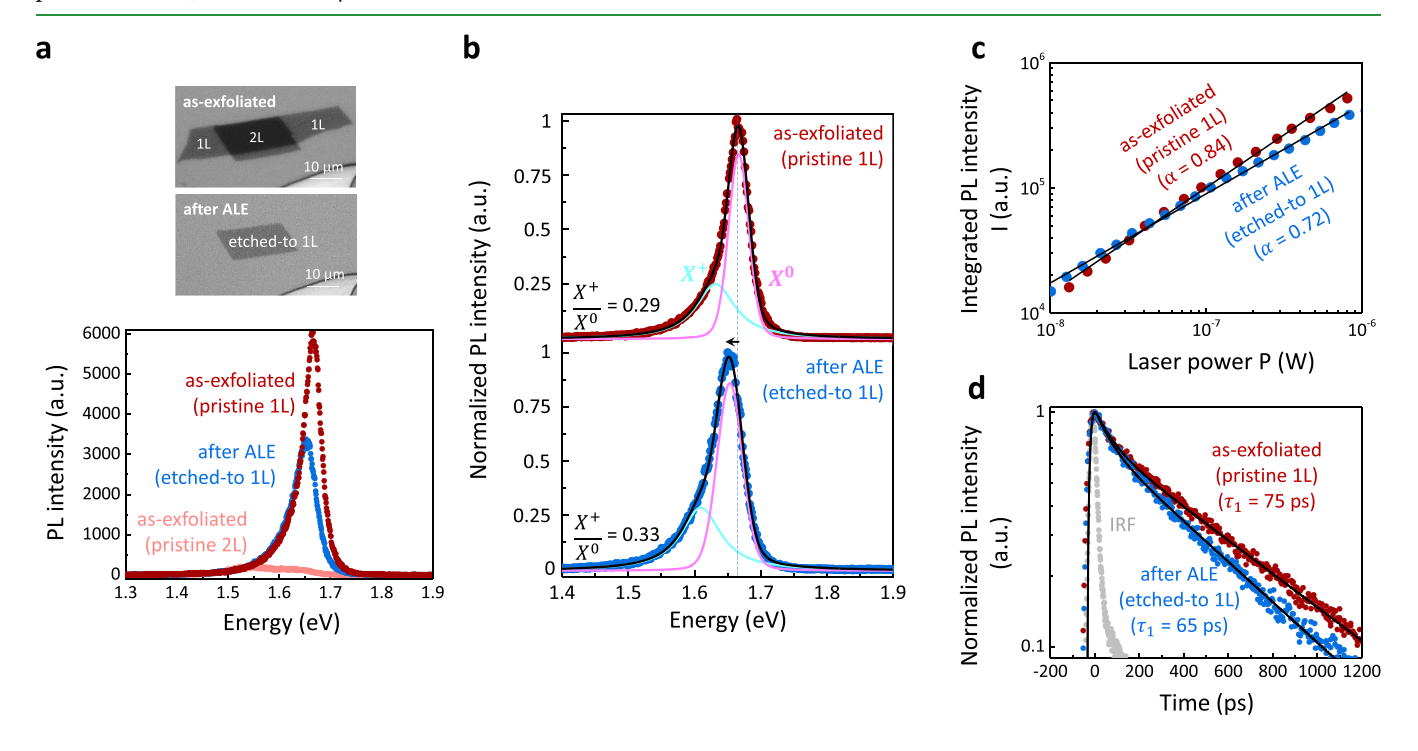


Figure 4. Optical characterization of etched-to 1L WSe₂. (a) Optical (gray-scaled) images of pristine WSe₂ flake (before and after etch) show that only one layer is removed per ALE cycle. Corresponding PL spectra confirm this with a clear transition from a broad low-intensity bilayer WSe₂ spectrum to a sharp monolayer spectrum for etched-to 1L WSe₂ after the ALE process. The etched-to 1L WSe₂ flake depicts PL characteristics similar to the pristine 1L WSe₂ flake with a 0.55× reduction in the peak PL intensity. (b) Deconvolved room-temperature PL spectra of the pristine and etched-to 1L WSe₂ from (a). The PL spectrum for the etched-to 1L WSe₂ shows the same number of deconvolved peaks (exciton peak (X^0) and hole trion peak (X^+) and similar X^+/X^0 ratio. (c) Integrated PL intensity (I) for as-exfoliated and etched-to monolayers for different pump laser powers (P). Both as-exfoliated and etched-to flakes show a similar sub-linear behavior. (d) Time-resolved PL decay also corroborates the similar optical characteristics of pristine and etched-1L WSe₂ flakes with comparable PL dynamics and decay time constants (τ).

also shows self-limiting oxidation and monolayer etching on MoSe₂ with no discernible damage while it does not show uniform oxidation on sulfide-based TMDCs (MoS₂ and WS₂) as shown in Figure S6. Thus, further theoretical studies are required to understand the difference between the oxygen passivating strength of transition metal sulfides and selenides. For WSe₂, we then selectively remove the only top oxidized layer using the etching step, further supporting our hypothesis. Thus, our PL characterization corroborates our optical, AFM, and Raman measurements and show that our ALE process removes precisely one layer per cycle.

Having established the monolayer precision of the ALE process, we then characterized optical, electrical, and material properties of etched-to flakes (also referred as ALE-processed flakes) and compared them to pristine (as-exfoliated) flakes of similar thickness. The quality of ALE-processed layers needs to be comparable to exfoliated or CVD-grown layers for use in 2D devices. The optical images in Figure 3a(i) shows clear thinning of the bilayer region to the monolayer after the ALE process along with the complete removal of the pristine monolayer region. The corresponding high-resolution AFM images, shown in Figure 3a(ii), further support the premise of atomic layer etching. The AFM image of the etched flake clearly shows that the ALE process is highly uniform with no apparent damage. This is different to previous oxidationenabled etching studies where large etch pits were formed on the flakes after the etching process. Note that the slight increase in (~1 Å) in the root mean square value of surface roughness (R_q) in the etched-to monolayer can also be attributed to substrate etching due to intercalated KOH as long-term KOH exposure leads to flake liftoff.

Figure 3b compares the normalized Raman spectrum of the etched-to monolayer WSe2 with that of the as-exfoliated flake. No additional peaks were observed in the etched-to monolayer, indicating pure hexagonal symmetry in the etched layers and the lack of macroscopic defects.⁴⁰ We used Gaussian-Lorentzian fits to deconvolve the curve into three distinct peaks, identified as A_{1g} (cyan), E_{2g}^1 (pink), and 2LA(M)(green). Compared to the pristine monolayer, all three peaks A_{1o} , E_{2o}^1 and 2LA(M) are slightly blueshifted by 0.14, 0.14, and 0.31 cm⁻¹, respectively. These small blueshifts are likely due to residual p-type doping and sample inhomogeneity. Finally, we also performed scanning transmission electron microscopy (STEM) and electron diffraction studies of etched-to and pristine 1L WSe₂ samples, as shown in Figure 3c. The STEM characterization bolsters our Raman measurements by showing the single-crystal nature of etched-to 1L flakes without any discernible defects or damage. Moreover, the diffraction patterns (shown in the inset) of the etched-to and pristine 1L flake show similar distance and angle between the adjacent planes suggesting similar hexagonal symmetry. Thus, the Raman spectrum and STEM characterization confirms that the ALE process maintains the quality of the etched-to monolayers.

Next, we performed room-temperature PL characterization to compare the optical quality of etched-to (2L to 1L) and pristine monolayers. The top panel of Figure 4a shows the optical image of an exfoliated WSe₂ flake with both monolayer and bilayer regions. The optical images clearly show the etching of the bilayer region to monolayer, which is further supported by the PL spectra given in the lower panel that shows a large increase in PL intensity after etching. We also performed hyperspectral mapping of the entire flake, before

and after etching, to determine the uniformity of the etch.⁴² As shown in Figure S7, the ALE technique provides a homogeneous etch with less than 20 meV variation in the PL spectral median over the entire etched flake. The PL intensity variation in the etched-to flake is similar to that of the as-exfoliated monolayer flake. After confirming the atomic layer etch, we compared the PL spectra of as-exfoliated and etched-to monolayer as shown in the lower panel of Figure 4a. Both spectra show similar PL characteristics with no additional features in the etched-to monolayer spectrum, except a small reduction in the peak PL intensity (~0.55×).

We then used Gaussian-Lorentzian fits to extract different excitonic components within the normalized PL spectra, as shown in Figure 4b. For as-exfoliated monolayer, a highintensity peak was observed at 1.67 eV with a linewidth of 36 meV that corresponds to a neutral exciton (X^0) peak for roomtemperature measurements. Along with that, a low-intensity shoulder peak occurs at 1.63 eV with a much larger linewidth of 70 meV that is attributed to positively charged trions (X^{+}) (two holes and one electron). 43 Compared to the as-exfoliated monolayer, we see no apparent change in the intensity of the X^0 peak except a small redshift (12 meV) and increase in linewidth (9 meV). The increase in linewidth can be attributed to several factors such as exciton-defect scattering, sample inhomogeneity, and residual doping. To rule out the role of exciton-defect scattering, we performed temperature-dependent PL measurements on pristine and etched-to flakes, provided in Figure S8. We observe no discernible defect peaks even at low temperatures (77 K), further supporting our claim of defect-free etch. Furthermore, the difference between the excitonic linewidth for pristine and etched-to monolayer reduces with lowering of temperature, which indicates slightly increased sample inhomogeneity in etched-to monolayers leading to larger excitonic linewidths. To understand the role of residual doping, we adopted the study from McCreary et al. where the shoulder to main peak intensity ratio was presented as an important quantitative parameter to determine the pristine nature of any 2D material.⁴⁴ We observe a slight increase in X^+/X^0 ratio (0.29-0.33) in the etched-to monolayer indicating minimal residual doping, however substantially better than previous works where this ratio almost doubles after etching.⁴³

Furthermore, we performed power-dependent and timeresolved PL characterization on the same flake to obtain insights into the dynamic behavior of PL characteristics in the etched-to layer compared to that of the pristine WSe₂ layer. Figure 4c shows a log-log plot of the integrated PL intensity (I) as a function of laser power (P) for both as-exfoliated (pristine) and etched-to monolayers. These logarithmic plots can be described by the power-law equation, i.e., $I \propto P^{\alpha}$, where α represents the linearity factor. For exciton-dominant (X^0) PL, α is close to unity at a low excitation power (<1.5 μ W) due to radiative recombination processes governed by a first-order rate equation. However, in the presence of defects, the linearity factor deviates from this ideal value and either becomes highly sublinear ($\alpha = 0.3$) or superlinear ($\alpha = 1.45$), as shown in previous studies. Here, we extracted $\alpha = 0.72$ for the etched-to monolayers, which is similar to that of the pristine monolayer (α = 0.84). As discussed before, the slight reduction in the α value can also be attributed to higher sample inhomogeneity and trion (hole doping) concentration in the etched-to monolayer compared to the pristine monolayer.⁴⁸ Thus, we do not observe a significant reduction or increase in

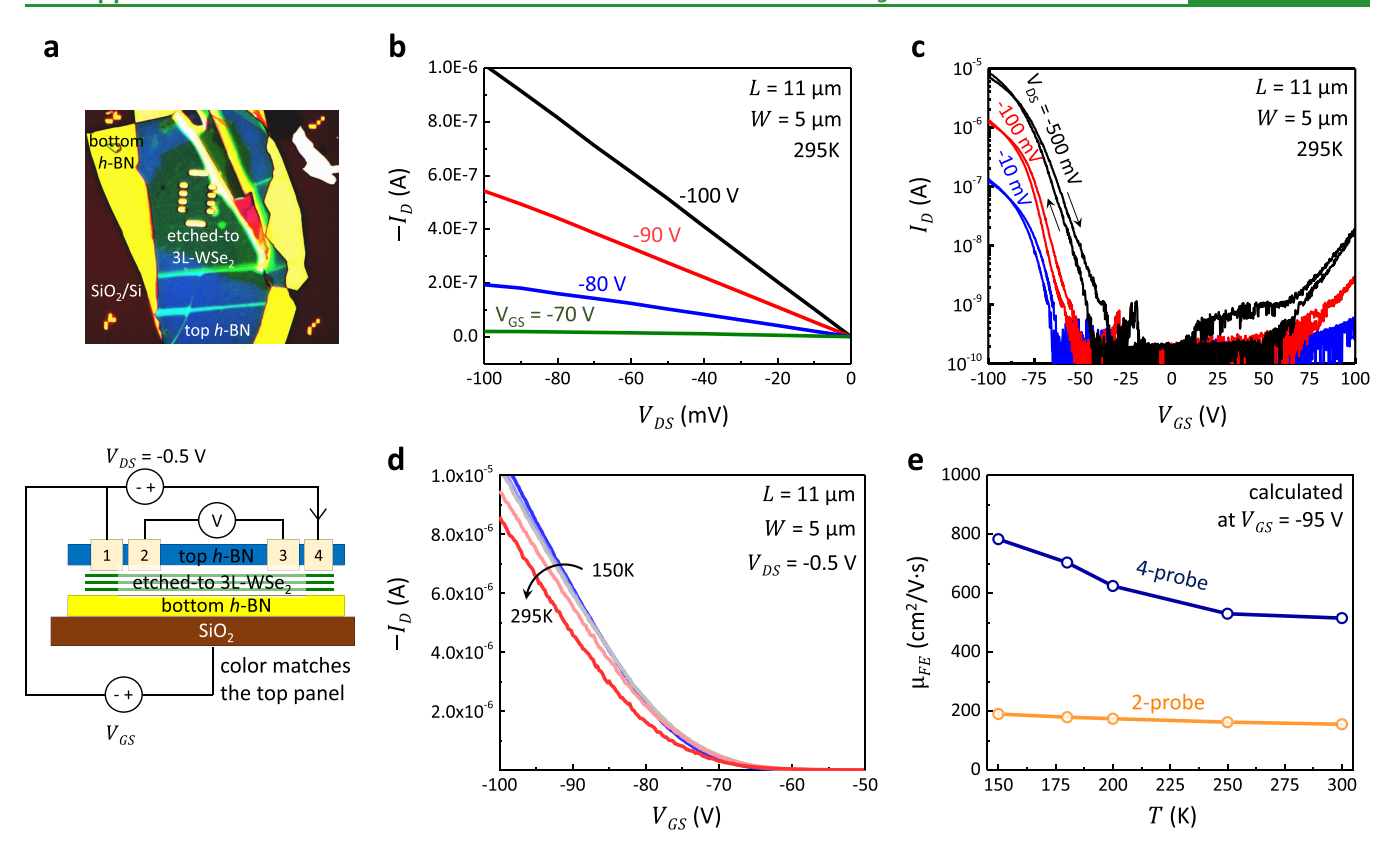


Figure 5. Electrical properties of ALE-processed WSe₂ flakes. (a) Color-corrected optical image (top panel) and device schematic (bottom panel) of a back-gated 2D device made from an etched-to 3L WSe₂ flake with transferred via contacts made from Pt in a Hall-bar pattern. The WSe₂ was exfoliated as a 5L flake and etched-to 3L using two cycles of the ALE process. (b) Output characteristics show a linear behavior at low $V_{\rm DS}$ values for high gate voltages. (c) Transfer characteristics show good p-type conduction with a high ON current, low hysteresis, and large ON/OFF ratio. (d) Temperature-dependent transfer characteristics showing the linear region of device operation for $V_{\rm GS} < -80\,\rm V$. (e) Extracted two (2)-probe and four (4) probe field-effect mobility ($\mu_{\rm FE}$) at $V_{\rm GS} = -95\,\rm V$ at different temperatures. A high four-probe hole mobility of 515 cm²/V·s at room temperature denotes the high-quality electrical properties of ALE-processed WSe₂ flakes.

the α , further confirming the nearly defect-free nature of the etched-to monolayers.

Figure 4d shows the normalized time-resolved PL decay for both as-exfoliated and etched-to monolayers. Here, IRF stands for instrument response function, which indicates the limits of the measurement system (~20 ps). We used Gaussianbiexponential fits to extract fast (τ_1) and slow (τ_2) decay time constants, where τ_1 is associated with the dynamics of bright exciton, and τ_2 is associated with dark exciton. The fast decay constant decreases slightly from 75 ps in the pristine monolayer to 65 ps in etched-to monolayer, suggesting similar exciton recombination dynamics in both. Since we do not see any discernible defects in temperature-dependent PL, the slight decrease once again indicates larger sample inhomogeneity and trion density in the etched-to monolayer. Thus, our detailed PL characterization supports our claim that the optical (PL) properties (both static and dynamic) of ALE-processed flakes are comparable to pristine WSe₂ layers.

Next, we investigated the electrical properties of ALE-processed WSe $_2$ flakes by fabricating an ideal p-type transistor, one of the most prominent applications of WSe $_2$. For this, we fabricated a back-gated field-effect transistor on an ALE-processed trilayer (3L) WSe $_2$ flake, back-gated through a \sim 60 nm h-BN /285 nm SiO $_2$ dielectric stack, as shown in Figure 5a. The 3L WSe $_2$ flake was obtained from an as-exfoliated 5L flake by performing two cycles of ALE process. We chose 3L WSe $_2$ for our study as (i) thick flakes (>10 layer) are largely

unaffected by etch processes since the majority of current flow occurs in the bottom layers and (ii) 1L/2L WSe $_2$ devices are limited by high contact resistance resulting in mainly n-type transport even with high work function metals. Fo,51 To illustrate this, we fabricated pristine and etched-to 1L WSe $_2$ devices, shown in Figure S9, which depicts similar n-dominant ambipolar characteristics for both devices. Moreover, the devices show extremely small ON currents at large negative V_{GS} values, illustrating the need of a different contacting technique to study the inherent p-type transport in WSe $_2$. Therefore, to obtain high-quality p-type contacts, we used a newly developed technique called transferred via contacts consisting of platinum (Pt) embedded in h-BN vias patterned in a Hall-bar structure.

Figure 5b shows the output characteristics of the device for low $V_{\rm DS}$ values indicating a linear behavior at high gate voltages, which is useful for extracting accurate field-effect mobilities. The transfer characteristics, shown in Figure 5c, depict a high ON current (~10 μ A at $V_{\rm DS}=-500$ mV), excellent ON/OFF ratio (10^5 , limited by the 100 pA leakage floor of our measurement setup), good sub-threshold swing, and small hysteresis. Overall, the transfer characteristics highlight the excellent switching characteristics of the etchedto 3L WSe₂ layers. To further quantify the electrical properties of the ALE-processed WSe₂, we extracted temperature-dependent field-effect mobility ($\mu_{\rm FE}$) using four-probe measurements, as shown in the lower panel of Figure 5a.

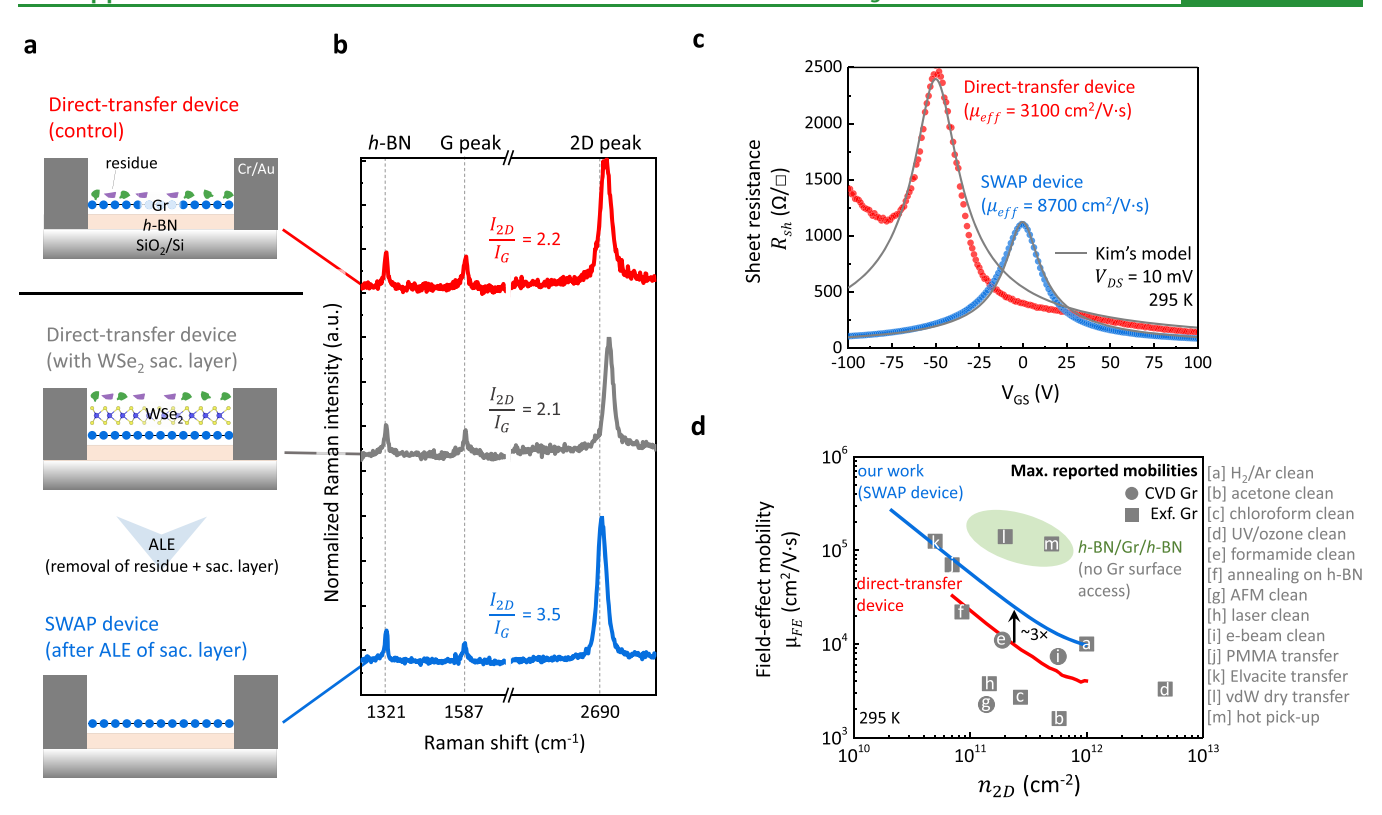


Figure 6. Sacrificial WSe₂ with ALE processing (SWAP) technique for high-quality 2D devices. (a) Schematic and process flow of a graphene device made with direct PCL transfer (control device) and using the SWAP technique. The ALE process removes the sacrificial WSe₂ layer along with the polymer residue accumulated in the transfer and lithography steps. (b) Raman measurements show the relative cleanliness of the samples. Raman spectra of the control device show a broadened 2D peak with a small $I_{\rm 2D}/I_{\rm G}$ ratio (2.2), indicating the presence of polymer residues on top of graphene. Raman spectra for the direct transfer device with the WSe₂ sacrificial layer has a sharper 2D peak, compared to that of the control device. The subsequent ALE process removes the top WSe₂ layer along with the polymer residue and leads to a clean graphene surface indicated by the large $I_{\rm 2D}/I_{\rm G}$ ratio, suggesting minimal damage to the underlying graphene layer during the ALE process. (c) Comparison of sheet resistance ($R_{\rm sh}$) for graphene devices made using direct transfer and the SWAP technique, showing better electrical characteristics of the SWAP device with a Dirac peak close to 0 V, a 2.5× reduction in $R_{\rm sh}$ at corresponding Dirac peaks, and a 3× increase in effective mobilities extracted using the Kim's model (dark gray lines). (d) Room-temperature four-probe field-effect mobility ($\mu_{\rm FE}$) of the device made using the SWAP technique shows a minimum 3× improvement at any carrier density ($n_{\rm 2D}$) over the devices fabricated with direct PCL transfer. The SWAP-enabled device shows better mobility than an unencapsulated graphene device.

The four-probe measurements enable us to measure both twoprobe and four-probe mobilities (corrected for contact resistance, $R_{\rm C}$). Figure 5d shows the temperature-dependent transfer characteristics at $V_{\rm DS}$ = - 500 mV from which we extracted two-probe and four-probe conductances, given in Figure S10a,b. We then extracted the field-effect mobilities from the respective two-probe and four-probe transconductances at $V_{\rm GS}$ = - 95 V, corresponding to the linear region of device operation. The extracted mobilities are shown in Figure 5e, and the corresponding hole sheet densities (p_{2D}) are given in Figure S10c. Further details of the mobility extraction technique are provided in the Supporting Information. For our 3L WSe₂ device, a room-temperature four-probe hole mobility of 515 cm²/V·s at $V_{GS} = -95$ V corresponding to $p_{2D} = 1.2 \times$ 1012 cm⁻² was extracted, which is the highest reported hole mobility in few (1-5)-layer WSe₂ devices. Table S1 compares the field-effect mobilities of our device with several other reported high-quality WSe2 devices, which shows that our ALE-processed flakes show similar or higher mobilities than pristine WSe₂-based devices. Note that, since the channel was not patterned in a Hall-bar geometry, we also calculated the variation in the extracted four-probe mobilities considering different electrical widths of the device, shown in Figure S10d.

Overall, our electrical characterization demonstrates the highelectrical quality of the ALE-processed WSe₂ flakes.

So far, we have demonstrated that our ALE process generates WSe₂ layers of desired thickness with comparable material and electrical properties to pristine flakes. Interestingly, we can also utilize the ALE process to provide a path for clean processing of 2D materials to enable high-performance devices. For enabling this, we use monolayer WSe2 as a sacrificial layer between the pickup polymer and the flake of interest. The monolayer WSe2 is subsequently etched after the transfer, leaving the desired material of interest in its pristine form without any polymer residue. Using graphene as a platform, we show that devices fabricated with our sacrificial WSe₂ layer with ALE processing (SWAP) technique retain a high electron/hole mobility. We illustrate the advantages of our ALE process in the clean fabrication of 2D devices by fabricating two sets of graphene devices: one without WSe2 (the control device) and another with the SWAP technique. Both devices were made using the previously mentioned PCL polymer-based dry transfer process. The control device was made using standard PCL transfer where graphene was picked up directly by PCL and transferred onto bottom h-BN. Although this process is much faster than other van der Waalsbased dry transfer processes, it results in significant polymer

residues on the transferred layer that is hard to remove even with best cleaning techniques such as vacuum annealing and AFM cleaning. Moreover, subsequent device processing, such as channel patterning and contact formation, leave additional resist and solvent residues that contaminates the channel. Figure 6a shows a schematic of the control device made using direct PCL transfer, indicating the presence of all kinds of residue on top of the graphene layer. Raman measurements, shown in Figure 6b, confirm the presence of significant residues (even after vacuum annealing) as indicated by a small cleanliness ratio (I_{2D}/I_G) of 2.2, similar to that of other unencapsulated devices made on graphene on top of h-BN.66

In our SWAP method, we first pick up monolayer WSe₂ with PCL polymer and then pick up monolayer graphene using the PCL/monolayer WSe₂ stack, which is finally transferred on bottom h-BN. Subsequently, the Gr/WSe₂ stack is patterned in a Hall-bar geometry and edge contacts are formed using the same etch mask. Thus, graphene remains in its pristine form and is not exposed to polymer along with clean patterning using standard lithographic techniques. Raman measurements of the device with WSe2 on top of graphene show smaller fullwidth at half maxima (FWHM) of the I_{2D} peak compared to that of the direct-transfer device, indicating a clean graphene-WSe₂ interface. Next, we use the ALE process to remove the top WSe₂ layer without altering the properties of underlying graphene. Only the top surface of the monolayer WSe₂ is exposed during device processing, so the ALE process removes this contamination along with the WSe₂ monolayer, leaving behind a pristine graphene surface. Raman measurements show that the $I_{\rm 2D}/I_{\rm G}$ ratio increases by 60% after the removal of WSe_2 (2.1-3.5) and becomes comparable to that of previously calculated values for pristine graphene (3-4), demonstrating the advantages of the SWAP technique.⁶⁷

Next, we performed electrical characterization to corroborate our claim of making high-quality graphene devices using our SWAP technique. Figure 6c compares the four-probe electrical characteristics of our SWAP device with the control sample, i.e., the direct-transfer device. As discussed earlier, four-probe characterization enables a comparison of the intrinsic properties of the channel layer without the effect of contact resistance. Here, the direct-transfer device shows a large shift in the Dirac voltage $(V_{\rm D})$ toward a negative gate voltage ($V_D = -50 \text{ V}$) along with a large sheet resistance (R_{sh}) away from the peak. This is also consistent with previous experimental works that show a large $V_{\rm D}$ shift and high $R_{\rm sh}$ values due to reduced carrier mobility and large residual doping due to polymer, photoresist, and solvent residue. 68,65 Note that our direct-transfer device shows n-type doping (negative V_D) compared to standard graphene devices made on SiO₂ due to the use of vacuum annealing and bottom h-BN, as shown in Figure S11. In contrast, the SWAP device shows nearly pristine characteristics with the Dirac point at $V_{GS} \approx 0 \text{ V}$ and a 2.5× reduction in $R_{\rm sh}$ at the corresponding Dirac voltage $(V_{\rm D})$. We further model the $R_{\rm sh}$ vs $V_{\rm GS}$ characteristics using the effective mobility method ($\mu_{\rm eff}$) provided by Kim et al., indicated by the corresponding solid (dark gray) lines. In this method, the gate only controls the carrier density in the device and thus the sheet resistance can be modeled as $R_{\rm sh}$ = $(q(n_{\rm eff}(V_{\rm GS})\mu_{\rm eff})^{-1}$, where q is the electron charge. The effective carrier density can be given as $n_{eff}(V_{GS}) =$ $\sqrt{(n(V_{\rm GS}-V_{\rm D}))^2+(n_0)^2}$, where n_0 is the residual doping density at the Dirac voltage. Using this method, we extract $\mu_{\rm eff}$

= 8700 cm²/V·s and n_0 = 6.23 × 10¹¹ cm⁻² for the SWAP device along with $\mu_{\rm eff}$ = 3100 cm²/V·s and n_0 = 8.73 × 10¹¹ cm⁻² for the direct-transfer device. Clearly, the SWAP device provides much better mobilities ($\sim 3\times$) and lower residual doping (\sim 30%) than the direct-transfer device, elucidating the importance of clean transfer and device patterning.

To further quantify this improvement, we extracted the room-temperature field-effect mobility (μ_{FE}) for the directtransfer and SWAP device using the technique described in previous graphene studies. 63,64 Details of the mobility extraction method is given in the Supporting Information. As shown in Figure 6d, the SWAP device illustrates a 3× increase in the field-effect mobility at any carrier density (n_{2D}) over the direct-transfer device, similar to the increase in $\mu_{\rm eff}$, thus highlighting the advantages of the SWAP technique. To compare the SWAP-enabled device with published results, we plotted the maximum field-effect mobility extracted for graphene devices made using different cleaning and transfer techniques. Our SWAP technique provides extremely high mobilities (~200,000 cm²/V·s), higher than any other unencapsulated device and below only to fully h-BN encapsulated graphene devices. Even though fully encapsulated graphene devices show better characteristics, the fabrication method is extremely slow and cannot be used for sensing applications and near-field measurements that require direct access to the surface of the devices. Thus, our SWAP technique provides a faster, cleaner, and reliable method to fabricate highquality 2D devices with no discernible degradation of pristine

EXPERIMENTAL SECTION

Details of XPS Characterization. Multilayer (4L) WSe₂ flakes were stacked on a thick h-BN flake by the dry transfer process using PCL polymer. The flakes were picked up at 50-58 °C and then transferred onto h-BN exfoliated on another 285 nm SiO₂/Si chip. Finally, the polymer was removed by first melting the polymer at 80 °C, followed by vacuum annealing at 340 °C. XPS measurements were obtained using the Physical Electronics VersaProbe II XPS tool utilizing a monochromated Al K α X-ray source ($h\nu$ = 1486.7 eV) with a spot size of 10 μ m in diameter in an ultrahigh vacuum chamber with a base pressure of $<10^{-9}$ Torr. The incident X-ray and analyzer were positioned at 45° to the sample. We used the scanning X-ray induced secondary electron imaging (SXI) capability of the tool to get data from the same flake in different runs. The carbon C 1s peak at 284.8 eV was used for binding energy calibration. The high-resolution XPS core-level spectra were analyzed after deconvolution using the leastsquares fitting of spectra with Voigt function (convolution of Gaussian and Lorentzian functions) after the Shirley background subtraction.

Details of Raman and PL Measurements. WSe2 flakes were first exfoliated on a SiO₂/Si substrate using mechanical exfoliation from a bulk crystal. AFM topography measurements were performed in air using the ScanAsyst mode of a Bruker Dimension AFM and then analyzed using the Bruker Nanoscope Analysis tool. Raman and PL measurements were performed using the Renishaw inVia confocal Raman microscope system in ambient air with an unpolarized 532 nm laser excitation and 100× magnification objective (NA = 0.90) giving a laser spot size of 1 μ m in diameter. Raman spectra were obtained at a laser power of 100 μW with a 1800 lines/mm grating. Raman spectra were calibrated with the Raman signature of Si at 520 cm⁻¹. All Raman spectra were deconvoluted using the Voigt function. PL spectra were collected at a laser power of 20 μ W with a 1800 lines/ mm grating having an integration time of 10 s. Voigt fitting was applied to deconvolute the PL spectra.

Details of Hyperspectral Imaging for Power-Dependent and Time-Resolved PL. Hyperspectral imaging is performed with

diffraction-limited spatial resolution, using a home-built multimodal confocal microscope. ⁴² Briefly, a Ti:sapphire laser (120 fs pulse, 80 MHz repetition rate) is used as the excitation source and focused onto the sample with an 100× objective with NA = 0.95. Emission signals are collected with back-scattering geometry, dispersed by a blazed grating (150 g/mm), and detected using an electron-magnifying CCD camera. Laser power is precisely controlled and automatically scanned using neutral density filters. For time-resolved measurements, signals are detected by a fast avalanche photodiode, which is synchronized to the laser pulses using the time-correlated single photon counting

Temperature-Dependent PL Measurements. Temperaturedependent PL measurements were done in our home-built scanning confocal microscope. A 460 nm CW diode laser was used as a pump through a 20×, 0.42 NA objective, and the collected back-scattered PL was detected using a liquid nitrogen cooled Horiba Symphony II detector. A 473 nm longpass filter was used in the output path to block the pump.

Fabrication and Electrical Characterization of WSe2 Transistors. The fabrication process starts with making the transferred via contacts. 52 For this, h-BN flakes were exfoliated onto a SiO₂/Si substrate outside the glovebox. Metal patterns were made using PMMA resist and Nanobeam NBL electron-beam lithography followed by trench formation using reactive-ion etch using the Oxford Plasma Pro 100 Cobra system with a 30/10 sccm flow of SF₆/ O2 gas at 20 W power for 1 min. Then, 20 nm Pt/30 nm Au was deposited in the trenches using electron-beam evaporation followed by metal liftoff using acetone. The transferred via contacts were then moved into the glovebox for further transfer process. In parallel, exfoliated WSe₂ is first stacked on bottom h-BN outside the glovebox by the dry-transferred, flip-chip method. For dry transfer, bottom h-BN is first picked up using a PDMS stamp coated with PPC polymer at 50 °C followed by a similar pickup for 5L WSe2. The PPC film is then stripped off from the underlying PDMS stamp and then transferred onto a separate SiO₂/Si chip in a flipped manner and then vacuum annealed to remove the underlying polymer. This stack is then processed using the ALE method and etched down to 3L WSe₂ by two cycles of the ALE. Subsequently, the transferred via contacts are transferred on top of this etched stack using the same pickup and transfer process inside a nitrogen glovebox. The top PPC is then washed away using acetone. Finally, metal contacts and measurement pads were made using EBL patterning and e-beam evaporation. All electrical measurements were performed in vacuum ($<1 \times 10^{-4}$ Torr) using a Keysight B1500A parameter analyzer.

Fabrication and Characterization of Graphene Device. Similar to the WSe2 transistor, all different 2D materials were first exfoliated on different SiO₂/Si substrates. We then find monolayer WSe₂ and graphene using an optical microscope. The stacking starts with the pickup of monolayer WSe2 with a PDMS stamp coated with PCL followed by another pickup of monolayer graphene. The stack is then transferred on bottom h-BN followed by stripping of the top polymer using vacuum annealing at 340 °C. After the stack is formed, edge contacts of Cr/Au (2 nm/80 nm) are made to the graphene layer using an e-beam evaporated metal after etching graphene using a CHF3-based RIE process. The use of the same PMMA mask for etching and metallization leads to easy formation of edge contacts to graphene. We then used the ALE process to remove the top WSe2 layer. The devices were then annealed at 300 °C to remove any residue on the top before moving into a vacuum probe station.

CONCLUSIONS

In this work, we present a clean, selective, and repeatable atomic layer etch for achieving high-quality WSe2 flakes of a required layer thickness. Using a comprehensive set of optical, material, and electrical characterization techniques, we provided a detailed characterization of the ALE-processed WSe₂ layers and benchmarked them against pristine (asexfoliated) flakes. Our ALE process provides etched flakes with minimal (if any) degradation in electrical and optical

properties and that are therefore much better than processed flakes that typically include contamination from polymers, solvents, and photoresist. We further use our ALE technique to demonstrate the fabrication of pristine high-quality 2D devices using WSe₂ as a sacrificial 2D layer. We show that graphene transistors protected by a sacrificial monolayer of WSe₂, which is subsequently removed using our ALE process, have a higher mobility than any other unencapsulated graphene device. Thus, our ALE process provides a path toward a controllable, and selective etch that can enable integration of 2D materials in CMOS technology for future applications.

ASSOCIATED CONTENT

Supporting Information

The Supporting Information is available free of charge at https://pubs.acs.org/doi/10.1021/acsami.0c18390.

Optical and AFM characterization of monolayer etchedto 1L WSe₂ before and after oxidation; Raman characterization indicating the amorphous nature of the TOS layer; Optical characterization to demonstrate the repeatability and patternability of the ALE process; AFM height mapping of etched-to 1L WSe₂ flakes; application of the ALE process to other TMDCs; hyperspectral mapping of photoluminescence spectra of exfoliated and etched flakes; temperature-dependent PL characterization of etched-to 1L WSe2; electrical characteristics of etched-to 1L WSe2 devices; temperature-dependent electrical characteristics of etched-to 3L WSe₂ devices; mobility extraction in WSe₂-based transistors; and substrate effects on electrical properties of graphene devices and mobility extraction in graphene transistors (PDF)

AUTHOR INFORMATION

Corresponding Authors

Ankur Nipane - Department of Electrical Engineering, Columbia University, New York 10027-6902, United States; orcid.org/0000-0003-2226-267X;

Email: ankur.nipane@columbia.edu

Min Sup Choi - Department of Mechanical Engineering, Columbia University, New York 10027-6902, United States; SKKU Advanced Institute of Nano Technology, Sungkyunkwan University, Suwon, Gyeonggi-do 16419, *Korea*; orcid.org/0000-0002-8448-4043;

Email: mc3614@columbia.edu

James T. Teherani – Department of Electrical Engineering, Columbia University, New York 10027-6902, United States; Email: j.teherani@columbia.edu

Authors

Punnu Jose Sebastian – Department of Electrical Engineering, Columbia University, New York 10027-6902, United States Kaiyuan Yao – Department of Mechanical Engineering, Columbia University, New York 10027-6902, United States Abhinandan Borah - Department of Electrical Engineering, Columbia University, New York 10027-6902, United States Prathmesh Deshmukh – Department of Physics, Graduate Center of the City University of New York, New York 10031-9101, United States

Younghun Jung - Department of Mechanical Engineering, Columbia University, New York 10027-6902, United States

- Bumho Kim Department of Mechanical Engineering, Columbia University, New York 10027-6902, United States
- Anjaly Rajendran Department of Electrical Engineering, Columbia University, New York 10027-6902, United States
- Kevin W. C. Kwock Department of Electrical Engineering, Columbia University, New York 10027-6902, United States
- Amirali Zangiabadi Department of Applied Physics and Mathematics, Columbia University, New York 10027-6902, United States
- Vinod M. Menon Department of Physics, Graduate Center of the City University of New York, New York 10031-9101, United States; orcid.org/0000-0002-9725-6445
- P. James Schuck Department of Mechanical Engineering, Columbia University, New York 10027-6902, United States; orcid.org/0000-0001-9244-2671
- Won Jong Yoo SKKU Advanced Institute of Nano Technology, Sungkyunkwan University, Suwon, Gyeonggi-do 16419, Korea; orcid.org/0000-0002-3767-7969
- James Hone Department of Mechanical Engineering, Columbia University, New York 10027-6902, United States

Complete contact information is available at: https://pubs.acs.org/10.1021/acsami.0c18390

Author Contributions

¹A.N. and M.S.C. lead the efforts on fabrication, characterization and data interpretation of ALE processed flakes under J.H. and J.T.T.'s supervision. P.J.S. developed the etch recipe and performed initial experiments. K.Y. performed the PL measurements of WSe₂ under P.J.S.'s supervision. A.B. supported the WSe₂ device fabrication and electrical measurements. P.D. performed the temperature-dependent PL measurements of WSe2 under V.M.M.'s supervision. Y.J. supported the electrical measurements of graphene devices. B.K. and A.Z. contributed to the preparation and measurements of samples for STEM and electron diffraction patterns. A.R. and K.W.C.K. studied and characterized the ALE process on other TMDCs. W.J.Y. contributed to the discussion of results and provided essential feedback. The manuscript was written by A.N., M.S.C., and J.T.T. with contributions of all authors. All authors have given approval to the final version of the manuscript.

Notes

The authors declare no competing financial interest.

ACKNOWLEDGMENTS

This work is supported by the National Science Foundation through CAREER Award (ECCS-1752401) and the Center for Precision Assembly of Superstratic and Superatomic Solids (DMR-1420634). This work is also supported by the National Research Foundation of Korea through the Global Research Laboratory (GRL) program (2016K1A1A2912707) and Research Fellow program (2018R1A6A3A11045864). This work was performed in part at the Advanced Science Research Center NanoFabrication Facility at the Graduate Center of the City University of New York.

REFERENCES

- (1) Li, X.-L.; Han, W.-P.; Wu, J.-B.; Qiao, X.-F.; Zhang, J.; Tan, P.-H. Layer-Number Dependent Optical Properties of 2D Materials and Their Application for Thickness Determination. *Adv. Funct. Mater.* **2017**, 27, 1604468–1604491.
- (2) Bae, J. J.; Jeong, H. Y.; Han, G. H.; Kim, J.; Kim, H.; Kim, M. S.; Moon, B. H.; Lim, S. C.; Lee, Y. H. Thickness-Dependent In-Plane

- Thermal Conductivity of Suspended MoS₂ Grown by Chemical Vapor Deposition. *Nanoscale* **2017**, *9*, 2541–2547.
- (3) Kanarik, K. J.; Tan, S.; Gottscho, R. A. Atomic Layer Etching: Rethinking the Art of Etch. *J. Phys. Chem Lett.* **2018**, *9*, 4814–4821.
- (4) He, T.; Wang, Z.; Zhong, F.; Fang, H.; Wang, P.; Hu, W. Etching Techniques in 2D Materials. *Adv. Mater. Technol.* **2019**, *4*, 1900064–1900082.
- (5) Stanford, M. G.; Rack, P. D.; Jariwala, D. Emerging Nanofabrication and Quantum Confinement Techniques for 2D Materials Beyond Graphene. *npj* 2D Mater. Appl. 2018, 2, 20.
- (6) Hu, L.; Shan, X.; Wu, Y.; Zhao, J.; Lu, X. Laser Thinning and Patterning of MoS₂ with Layer-by-Layer Precision. *Sci. Rep.* **2017**, *7*, 15538.
- (7) Castellanos-Gomez, A.; Barkelid, M.; Goossens, A. M.; Calado, V. E.; van der Zant, H. S. J.; Steele, G. A. Laser-Thinning of MoS₂: On Demand Generation of a Single-Layer Semiconductor. *Nano Lett.* **2012**, *12*, 3187–3192.
- (8) Huang, Y.; Wu, J.; Xu, X.; Ho, Y.; Ni, G.; Zou, Q.; Koon, G. K. W.; Zhao, W.; Castro Neto, A. H.; Eda, G.; Shen, C.; Özyilmaz, B. An Innovative Way of Etching MoS₂: Characterization and Mechanistic Investigation. *Nano Res.* **2013**, *6*, 200–207.
- (9) Yamamoto, M.; Dutta, S.; Aikawa, S.; Nakaharai, S.; Wakabayashi, K.; Fuhrer, M. S.; Ueno, K.; Tsukagoshi, K. Self-Limiting Layer-by-Layer Oxidation of Atomically Thin WSe₂. *Nano Lett.* **2015**, *15*, 2067–2073.
- (10) Balden, M.; Roth, J. New Weight-Loss Measurements of The Chemical Erosion Yields of Carbon Materials Under Hydrogen Ion Bombardment. *J. Nucl. Mater.* **2000**, 280, 39–44.
- (11) Xie, L.; Jiao, L.; Dai, H. Selective Etching of Graphene Edges by Hydrogen Plasma. *J. Am. Chem. Soc.* **2010**, *132*, 14751–14753.
- (12) Diankov, G.; Neumann, M.; Goldhaber-Gordon, D. Extreme Monolayer-Selectivity of Hydrogen-Plasma Reactions with Graphene. *ACS Nano* **2013**, *7*, 1324–1332.
- (13) Neyts, E. C.; Ostrikov, K.; Han, Z. J.; Kumar, S.; van Duin, A. C. T.; Bogaerts, A. Defect Healing and Enhanced Nucleation of Carbon Nanotubes by Low-Energy Ion Bombardment. *Phys. Rev. Lett.* **2013**, *110*, No. 065501.
- (14) Tsai, C.; Li, H.; Park, S.; Park, J.; Han, H. S.; Nørskov, J. K.; Zheng, X.; Abild-Pedersen, F. Electrochemical Generation of Sulfur Vacancies in The Basal Plane of MoS₂ for Hydrogen Evolution. *Nat. Commun.* **2017**, *8*, 15113.
- (15) Wang, Z.; Li, Q.; Xu, H.; Dahl-Petersen, C.; Yang, Q.; Cheng, D.; Cao, D.; Besenbacher, F.; Lauritsen, J. V.; Helveg, S.; Dong, M. Controllable Etching of MoS₂ Basal Planes for Enhanced Hydrogen Evolution Through The Formation of Active Edge Sites. *Nano Energy* **2018**, *49*, 634–643.
- (16) Wang, C.; Lu, H.; Tang, K.; Mao, Z.; Li, Q.; Wang, X.; Yan, C. Atom Removal on The Basal Plane of Layered MoS₂ Leading to Extraordinarily Enhanced Electrocatalytic Performance. *Electrochim. Acta* **2020**, 336, 135740–135749.
- (17) Yang, X.; Tang, S.; Ding, G.; Xie, X.; Jiang, M.; Huang, F. Layer-by-Layer Thinning of Graphene by Plasma Irradiation and Post-Annealing. *Nanotechnology* **2011**, *23*, 025704–025710.
- (18) Kim, K. S.; Ji, Y. J.; Nam, Y.; Kim, K. H.; Singh, E.; Lee, J. Y.; Yeom, G. Y. Atomic Layer Etching of Graphene Through Controlled Ion Beam for Graphene-Based Electronics. *Sci. Rep.* **2017**, *7*, 2462.
- (19) Liu, Y.; Nan, H.; Wu, X.; Pan, W.; Wang, W.; Bai, J.; Zhao, W.; Sun, L.; Wang, X.; Ni, Z. Layer-by-Layer Thinning of MoS₂ by Plasma. *ACS Nano* **2013**, *7*, 4202–4209.
- (20) Jeon, M. H.; Ahn, C.; Kim, H.; Kim, K. N.; LiN, T. Z.; Qin, H.; Kim, Y.; Lee, S.; Kim, T.; Yeom, G. Y. Controlled MoS_2 Layer Etching Using CF_4 Plasma. *Nanotechnology* **2015**, *26*, 355706–355714.
- (21) Xiao, S.; Xiao, P.; Zhang, X.; Yan, D.; Gu, X.; Qin, F.; Ni, Z.; Han, Z. J.; Ostrikov, K. K. Atomic-Layer Soft Plasma Etching of MoS₂. Sci. Rep. **2016**, 6, 1–8.
- (22) Zhu, H.; Qin, X.; Cheng, L.; Azcatl, A.; Kim, J.; Wallace, R. M. Remote Plasma Oxidation and Atomic Layer Etching of MoS₂. ACS Appl. Mater. Interfaces **2016**, 8, 19119–19126.

- (23) Kim, K. S.; Kim, K. H.; Nam, Y.; Jeon, J.; Yim, S.; Singh, E.; Lee, J. Y.; Lee, S. J.; Jung, Y. S.; Yeom, G. Y.; Kim, D. W. Atomic Layer Etching Mechanism of MoS₂ for Nanodevices. *ACS Appl. Mater. Interfaces* **2017**, *9*, 11967–11976.
- (24) Heyne, M. H.; Marinov, D.; Braithwaite, N.; Goodyear, A.; de Marneffe, J.-F.; Cooke, M.; Radu, I.; Neyts, E. C.; De Gendt, S. A Route Towards The Fabrication of 2D Heterostructures Using Atomic Layer Etching Combined With Selective Conversion. 2D Mater. 2019, 6, No. 035030.
- (25) Jain, A.; Bharadwaj, P.; Heeg, S.; Parzefall, M.; Taniguchi, T.; Watanabe, K.; Novotny, L. Minimizing Residues and Strain in 2D Materials Transferred From PDMS. *Nanotechnology* **2018**, 29, 265203–265212.
- (26) Son, S.; Shin, Y. J.; Zhang, K.; Shin, J.; Lee, S.; Idzuchi, H.; Coak, M. J.; Kim, H.; Kim, J.; Kim, J. H.; Kim, M.; Kim, D.; Kim, P.; Park, J.-G. Strongly Adhesive Dry Transfer Technique for Van Der Waals Heterostructure. 2D Mater. 2020, 7, No. 041005.
- (27) Zhao, P.; Kiriya, D.; Azcatl, A.; Zhang, C.; Tosun, M.; Liu, Y.-S.; Hettick, M.; Kang, J. S.; McDonnell, S.; Kc, S.; Guo, J.; Cho, K.; Wallace, R. M.; Javey, A. Air Stable p-Doping of WSe₂ by Covalent Functionalization. *ACS Nano* **2014**, *8*, 10808–10814.
- (28) Nipane, A.; Karmakar, D.; Kaushik, N.; Karande, S.; Lodha, S. Few-Layer MoS₂p-Type Devices Enabled by Selective Doping Using Low Energy Phosphorus Implantation. *ACS Nano* **2016**, *10*, 2128–2137.
- (29) Liu, Y.; Tan, C.; Chou, H.; Nayak, A.; Wu, D.; Ghosh, R.; Chang, H.-Y.; Hao, Y.; Wang, X.; Kim, J.-S.; Piner, R.; Ruoff, R. S.; Akinwande, D.; Lai, K. Thermal Oxidation of WSe₂ Nanosheets Adhered on SiO₂/Si Substrates. *Nano Lett.* **2015**, *15*, 4979–4984.
- (30) Li, Z.; Yang, S.; Dhall, R.; Kosmowska, E.; Shi, H.; Chatzakis, I.; Cronin, S. B. Layer Control of WSe₂ via Selective Surface Layer Oxidation. ACS Nano **2016**, 10, 6836–6842.
- (31) Zhao, Y.; Luo, X.; Li, H.; Zhang, J.; Araujo, P. T.; Gan, C. K.; Wu, J.; Zhang, H.; Quek, S. Y.; Dresselhaus, M. S.; Xiong, Q. Interlayer Breathing and Shear Modes in Few-Trilayer MoS₂ and WSe₂. *Nano Lett.* **2013**, *13*, 1007–1015.
- (32) Horzum, S.; Sahin, H.; Cahangirov, S.; Cudazzo, P.; Rubio, A.; Serin, T.; Peeters, F. M. Phonon Softening and Direct to Indirect Band Gap Crossover in Strained Single-Layer MoSe₂. *Phys. Rev. B* **2013**, 87, 125415–125420.
- (33) Mouri, S.; Miyauchi, Y.; Matsuda, K. Tunable Photoluminescence of Monolayer MoS₂ via Chemical Doping. *Nano Lett.* **2013**, *13*, 5944–5948.
- (34) Sen, H. S.; Sahin, H.; Peeters, F. M.; Durgun, E. Monolayers of MoS_2 as an Oxidation Protective Nanocoating Material. *J. Appl. Phys.* **2014**, *116*, 083508–083515.
- (35) Kc, S.; Longo, R. C.; Wallace, R. M.; Cho, K. Surface Oxidation Energetics and Kinetics on MoS₂ Monolayer. *J. Appl. Phys.* **2015**, *117*, 135301–135308.
- (36) Lee, C. H.; Lee, E. W., II; McCulloch, W.; Jamal-Eddine, Z.; Krishnamoorthy, S.; Newburger, M. J.; Kawakami, R. K.; Wu, Y.; Rajan, S. A Self-Limiting Layer-by-Layer Etching Technique for 2H-MoS₂. *Appl. Phys. Express* **2017**, *10*, 035201–035204.
- (37) Zheng, X.; Wei, Y.; Deng, C.; Huang, H.; Yu, Y.; Wang, G.; Peng, G.; Zhu, Z.; Zhang, Y.; Jiang, T.; Qin, S.; Zhang, R.; Zhang, X. Controlled Layer-by-Layer Oxidation of MoTe₂ via O₃ Exposure. *ACS Appl. Mater. Interfaces* **2018**, *10*, 30045–30050.
- (38) Yamamoto, M.; Einstein, T. L.; Fuhrer, M. S.; Cullen, W. G. Anisotropic Etching of Atomically Thin MoS₂. *J Phys. Chem.C* **2013**, 117, 25643–25649.
- (39) Ionescu, R.; George, A.; Ruiz, I.; Favors, Z.; Mutlu, Z.; Liu, C.; Ahmed, K.; Wu, R.; Jeong, J. S.; Zavala, L.; Mkhoyan, K. A.; Ozkan, M.; Ozkan, C. S. Oxygen Etching of Thick MoS₂ Films. *Chem. Commun.* **2014**, *50*, 11226–11229.
- (40) Sahin, H.; Tongay, S.; Horzum, S.; Fan, W.; Zhou, J.; Li, J.; Wu, J.; Peeters, F. M. Anomalous Raman Spectra and Thickness-Dependent Electronic Properties of WSe₂. *Phys. Rev. B* **2013**, 87, 165409–165415.

- (41) Pak, S.; Lee, J.; Lee, Y.-W.; Jang, A.-R.; Ahn, S.; Ma, K. Y.; Cho, Y.; Hong, J.; Lee, S.; Jeong, H. Y.; Im, H.; Shin, H. S.; Morris, S. M.; Cha, S.; Sohn, J. I.; Kim, J. M. Strain-Mediated Interlayer Coupling Effects on the Excitonic Behaviors in an Epitaxially Grown MoS₂/WS,van der Waals Heterobilayer. *Nano Lett.* **2017**, *17*, 5634–5640.
- (42) Yao, K.; Yanev, E.; Chuang, H.-J.; Rosenberger, M. R.; Xu, X.; Darlington, T.; McCreary, K. M.; Hanbicki, A. T.; Watanabe, K.; Taniguchi, T.; Jonker, B. T.; Zhu, X.; Basov, D. N.; Hone, J. C.; Schuck, P. J. Continuous Wave Sum Frequency Generation and Imaging of Monolayer and Heterobilayer Two-Dimensional Semiconductors. ACS Nano 2020, 14, 708–714.
- (43) Nam, H.-J.; Kim, J.; Park, J.-H. Wide-Range Controllable Doping of Tungsten Diselenide (WSe₂) based on Hydrochloric Acid Treatment. *J Phys. Chem.C* **2017**, *121*, 14367–14372.
- (44) McCreary, K. M.; Hanbicki, A. T.; Sivaram, S. V.; Jonker, B. T. A- and B-Exciton Photoluminescence Intensity Ratio As a Measure of Sample Quality for Transition Metal Dichalcogenide Monolayers. *APL Mater.* **2018**, *6*, 111106–111115.
- (45) Zhang, R.; Drysdale, D.; Koutsos, V.; Cheung, R. Controlled Layer Thinning and p-Type Doping of WSe₂ by Vapor XeF₂. Adv. Funct. Mater. **2017**, 27, 1702455–1702467.
- (46) Wu, Z.; Zhao, W.; Jiang, J.; Zheng, T.; You, Y.; Lu, J.; Ni, Z. Defect Activated Photoluminescence in WSe₂ Monolayer. *J. Phys. Chem. C* **2017**, *121*, 12294–12299.
- (47) Tanoh, A. O. A.; Alexander-Webber, J.; Xiao, J.; Delport, G.; Williams, C. A.; Bretscher, H.; Gauriot, N.; Allardice, J.; Pandya, R.; Fan, Y.; Li, Z.; Vignolini, S.; Stranks, S. D.; Hofmann, S.; Rao, A. Enhancing Photoluminescence and Mobilities in WS₂ Monolayers with Oleic Acid Ligands. *Nano Lett.* **2019**, *19*, 6299–6307.
- (48) Mak, K. F.; He, K.; Lee, C.; Lee, G. H.; Hone, J.; Heinz, T. F.; Shan, J. Tightly Bound Trions in Monolayer MoS₂. *Nat. Mater.* **2013**, 12, 207–211.
- (49) Movva, H. C. P.; Rai, A.; Kang, S.; Kim, K.; Fallahazad, B.; Taniguchi, T.; Watanabe, K.; Tutuc, E.; Banerjee, S. K. High-Mobility Holes in Dual-Gated WSe₂ Field-Effect Transistors. *ACS Nano* **2015**, *9*, 10402–10410.
- (50) Kaushik, N.; Nipane, A.; Basheer, F.; Dubey, S.; Grover, S.; Deshmukh, M.; Lodha, S. Evaluating Au and Pd Contacts in Mono and Multilayer MoS₂ Transistors. *72nd Device Research Conference*. IEEE 2014; pp 195–196
- (51) Prakash, A.; Ilatikhameneh, H.; Wu, P.; Appenzeller, J. Understanding Contact Gating in Schottky Barrier Transistors From 2D Channels. Sci. Rep. 2017, 7, 12596.
- (52) Jung, Y.; Choi, M. S.; Nipane, A.; Borah, A.; Kim, B.; Zangiabadi, A.; Taniguchi, T.; Watanabe, K.; Yoo, W. J.; Hone, J.; Teherani, J. T. Transferred Via Contacts As a Platform for Ideal Two-Dimensional Transistors. *Nat. Electron.* **2019**, *2*, 187–194.
- (53) Mitta, S. B.; Choi, M. S.; Nipane, A.; Ali, F.; Kim, C.; Teherani, J. T.; Hone, J.; Yoo, W. J. Electrical characterization of 2D materials-based field-effect transistors. 2D Materials 2020, 8, 012002–012030.
- (54) Yun, H.; Lee, S.; Jung, D.; Lee, G.; Park, J.; Kwon, O. J.; Lee, D. J.; Park, C.-Y. Removal of Photoresist Residues and Healing of Defects on Graphene Using H₂ and CH₄ plasma. *Appl. Surf. Sci.* **2019**, 463. 802–808.
- (55) Cheng, Z.; Zhou, Q.; Wang, C.; Li, Q.; Wang, C.; Fang, Y. Toward Intrinsic Graphene Surfaces: A Systematic Study on Thermal Annealing and Wet-Chemical Treatment of SiO₂ -Supported Graphene Devices. *Nano Lett.* **2011**, *11*, 767–771.
- (56) Li, W.; Liang, Y.; Yu, D.; Peng, L.; Pernstich, K. P.; Shen, T.; Hight Walker, A. R.; Cheng, G.; Hacker, C. A.; Richter, C. A.; Li, Q.; Gundlach, D. J.; Liang, X. Ultraviolet/Ozone Treatment to Reduce Metal-Graphene Contact Resistance. *Appl. Phys. Lett.* **2013**, *102*, 183110–183115.
- (57) Suk, J. W.; Lee, W. H.; Lee, J.; Chou, H.; Piner, R. D.; Hao, Y.; Akinwande, D.; Ruoff, R. S. Enhancement of the Electrical Properties of Graphene Grown by Chemical Vapor Deposition via Controlling the Effects of Polymer Residue. *Nano Lett.* **2013**, *13*, 1462–1467.
- (58) Gannett, W.; Regan, W.; Watanabe, K.; Taniguchi, T.; Crommie, M. F.; Zettl, A. Boron Nitride Substrates for High Mobility

- Chemical Vapor Deposited Graphene. Appl. Phys. Lett. 2011, 98, 242105-242107.
- (59) Boscá, A.; Pedrós, J.; Martínez, J.; Palacios, T.; Calle, F. Automatic Graphene Transfer System for Improved Material Quality and Efficiency. *Sci. Rep.* **2016**, *6*, 21676–21683.
- (60) Jia, Y.; Gong, X.; Peng, P.; Wang, Z.; Tian, Z.; Ren, L.; Fu, Y.; Zhang, H. Toward High Carrier Mobility and Low Contact Resistance: Laser Cleaning of PMMA Residues on Graphene Surfaces. *Nano-Micro Lett.* **2016**, *8*, 336–346.
- (61) Son, B. H.; Kim, H. S.; Jeong, H.; Park, J.-Y.; Lee, S.; Ahn, Y. H. Electron Beam Induced Removal of PMMA Layer Used for Graphene Transfer. *Sci. Rep.* **2017**, *7*, 18058.
- (62) Dean, C. R.; Young, A. F.; Meric, I.; Lee, C.; Wang, L.; Sorgenfrei, S.; Watanabe, K.; Taniguchi, T.; Kim, P.; Shepard, K. L.; Hone, J. Boron Nitride Substrates for High-Quality Graphene Electronics. *Nat. Nanotechnol.* **2010**, *5*, 722–726.
- (63) Zomer, P. J.; Dash, S. P.; Tombros, N.; van Wees, B. J. A Transfer Technique for High Mobility Graphene Devices on Commercially Available Hexagonal Boron Nitride. *Appl. Phys. Lett.* **2011**, 99, 232104–232107.
- (64) Wang, L.; Meric, I.; Huang, P. Y.; Gao, Q.; Gao, Y.; Tran, H.; Taniguchi, T.; Watanabe, K.; Campos, L. M.; Muller, D. A.; Guo, J.; Kim, P.; Hone, J.; Shepard, K. L.; Dean, C. R. One-Dimensional Electrical Contact to a Two-Dimensional Material. *Science* **2013**, *342*, 614–617.
- (65) Pizzocchero, F.; Gammelgaard, L.; Jessen, B. S.; Caridad, J. M.; Wang, L.; Hone, J.; Bøggild, P.; Booth, T. J. The Hot Pick-Up Technique for Batch Assembly of Van Der Waals Heterostructures. *Nat. Commun.* **2016**, *7*, 11894.
- (66) Lin, L.; Zhang, J.; Su, H.; Li, J.; Sun, L.; Wang, Z.; Xu, F.; Liu, C.; Lopatin, S.; Zhu, Y.; Jia, K.; Chen, S.; Rui, D.; Sun, J.; Xue, R.; Gao, P.; Kang, N.; Han, Y.; Xu, H. Q.; Cao, Y.; Novoselov, K. S.; Tian, Z.; Ren, B.; Peng, H.; Liu, Z. Towards Super-Clean Graphene. *Nat. Commun.* **2019**, *10*, 1912.
- (67) Wang, D.-Y.; Huang, I.-S.; Ho, P.-H.; Li, S.-S.; Yeh, Y.-C.; Wang, D.-W.; Chen, W.-L.; Lee, Y.-Y.; Chang, Y.-M.; Chen, C.-C.; Liang, C.-T.; Chen, C.-W. Clean-Lifting Transfer of Large-area Residual-Free Graphene Films. *Adv. Mater.* 2013, 25, 4521–4526.
- (68) Stehle, Y. Y.; Voylov, D.; Vlassiouk, I. V.; Lassiter, M. G.; Park, J.; Sharma, J. K.; Sokolov, A. P.; Polizos, G. Effect of Polymer Residues on the Electrical Properties of Large-Area Graphene-Hexagonal Boron Nitride Planar Heterostructures. *Nanotechnology* **2017**, *28*, 285601–285609.
- (69) Park, J.-H.; Jung, W.; Cho, D.; Seo, J.-T.; Moon, Y.; Woo, S. H.; Lee, C.; Park, C.-Y.; Ahn, J. R. Simple, Green, and Clean Removal of a Poly(methyl methacrylate) Film on Chemical Vapor Deposited Graphene. *Appl. Phys. Lett.* **2013**, *103*, 171609–171613.
- (70) Kim, S.; Nah, J.; Jo, I.; Shahrjerdi, D.; Colombo, L.; Yao, Z.; Tutuc, E.; Banerjee, S. K. Realization of a High Mobility Dual-Gated Graphene Field-Effect Transistor with A₂O₃ Dielectric. *Appl. Phys. Lett.* **2009**, *94*, 062107–062111.